Effect of nickel monolayer deposition on the structural and electronic properties of the low miller indices of (bcc) iron: A DFT study

Caroline R. Kwawu [a], Richard Tia [a,*], Evans Adei [a], Nelson Y. Dzade [b,*], C. Richard A. Catlow [c,d], Nora H. de Leeuw [b,c,d]

[a] Department of Chemistry, Kwame Nkrumah University of Science and Technology, Kumasi, Ghana
[b] Department of Earth Sciences, Utrecht University, Princetonplein 9, 3584 CC, Utrecht, The Netherlands [c] Department of Chemistry, University College London, 20 Gordon Street, WC1H 0AJ, London, UK
[d] School of Chemistry, Cardiff University, Main Building, Park PI, Cardiff CF10 3AT, UK

article info

Keywords:
Deposition
Surface relaxation
Surface reconstruction
Surface energies
Work function
Charge density difference
Projected density of states
Density functional theory

abstract

Metal clusters of both iron (Fe) and nickel (Ni) have been found in nature as active electro-catalytic sites, for example in the enzyme carbon mono-oxide dehydrogenase found in autotrophic organisms. Thus, surface modification of iron with nickel could improve the surface work function to enhance catalytic applications. The effects of surface modifications of iron by nickel on the structural and electronic properties have been studied using spin-polarised density functional theory calculations within the generalised gradient approximation. The thermodynamically preferred sites for Ni adsorption on the Fe (100), (110) and (111) surfaces have been studied at varying monolayer coverages (including 0.25 ML and 1 ML). The work function of the bare Fe surfaces is found to be of the order (100) ~ (111) < (110) i.e. 3.80 eV ~ 3.84 eV < 4.76 eV, which is consistent with earlier studies. The adsorption energies show that monolayer Ni deposition is thermodynamically favoured on the (100) and (111) surfaces, but not on the (110) surface. Expansion of the first interlayer spacing (d_{12}) of all three Fe surfaces is observed upon Ni deposition with the extent of expansion decreasing in the order (111) > (110) > (100), i.e. 6.78% > 5.76% > 1.99%. The extent of relaxation is magnified on the stepped (111) surface (by 1.09% to 30.88%), where the Ni coordination number is highest at 7 compared to 5 on the (100) facet and 4 on the (110) facet. The Ni deposition changes the work functions of the various surfaces due to charge reordering illustrated by charge density plots, where the work function is reduced only on the (110) surface by 0.04 eV, 0.16 eV and 0.17 eV at 1 ML, 0.5 ML and 0.25 ML respectively, with a concomitant increase in the surface dipole (polarity). This result implies enhanced electron activity and electrochemical reactivity on the most stable and therefore frequently occurring Ni-doped (110) facet compared to the clean (110) facet, which has implications for the development of improved Fe electro-catalysts (for example for CO_2 activation and reduction). These findings improve our understanding of the role of surface topology and stability on the extent of Ni interactions with Fe surfaces and the extent to which the Fe surface structures and properties are altered by the Ni deposition.

1. Introduction

Iron and nickel are known to be catalytically active sites for CO_2 reduction, for example in the enzyme carbon-monoxide dehydrogenase which is responsible for CO_2 conversion to CO under ambient conditions [1,2]. Moreover, Nerlov et al. [3] observed that nickel deposited on the copper (100) surface led to a 60-fold increase in the yield of methanol produced from CO_2, CO and H_2. More generally, iron is a relatively cheap material whose surface alteration could have important implications for catalysis, electro-chemistry and the prevention of corrosion.

The structural and hence electronic properties of surfaces differ from the bulk, not only due to the lower coordination of sur-face atoms but also due to relaxation and/or reconstruction of the surface [4]. Adsorbates may also induce surface relaxation and reconstruction, where surface atoms relocate to optimize the strength of adsorbate-substrate bonds, leading to the formation of new and unexpected surface structures and properties [5]. For

* Corresponding authors.
E-mail addresses: kwawucaroline@gmail.com (C.R. Kwawu), richtiagh@yahoo.com (R. Tia), N.Y.Dzade@uu.nl (N.Y. Dzade), DeLeeuwN@cardiff.ac.uk (N.H. de Leeuw).

example, Shih et al. [6] found that sulphur on Fe (110) leads to reconstruction of the surface.

Epitaxial growth, i.e. the deposition and growth of, for example, a metal with a certain crystal structure on another metal crystal has been widely studied. A review of experimental studies of epitaxial growth of Fe, Co, Ni and Cu on low Miller indices of bcc W and Mo [7] shows that the work function varies significantly as a function of facet, number of deposited atomic layers and deposition time. Deposition on other bcc surfaces such as Fe, Cr, V, Nb, and Ta has, however, remained relatively under-explored, partly due to the difficulty associated with cleaning these surfaces. One of the difficulties in cleaning iron surfaces is its transition from bcc to fcc at 1183 K [8].

Deposition and growth of nickel has been extensively studied on the bcc tungsten metal facets. Based on the differences in surface energies [9], ferromagnetic metals like Ni, Co and Fe are expected to grow by the Stranski-Krastanov growth at elevated temperatures and by the quasi-Frank-van der Merwe growth at lower tempera-tures, which requires an initial 1–2 pseudo-morphic monolayers. This growth pattern has already been seen for Ni deposits on W and Mo [10–18]. On the close-packed (110) facet, most of these experimental studies support the idea of structural changes before total surface coverage, from pseudo-morphic through distorted structures to close-packed fcc (110) structures beyond 1 ML coverage. These changes are supported by work function measurements [10], which are very sensitive to surface roughness and UPS spectra at energies sensitive to structural changes [12]. This suggests change in surface roughness with deposition coverage, whereas the work function changes are small after the completion of the first layer [10]. The early stages of Ni growth on W(100) has been studied along with the nickel-deposited W(110) facet, where the nickel first monolayer was reported to be pseudo-morphic with the sub-monolayers reconstructing due to anisotropic misfit and strain on the film [17]. Using ultra-high vacuum (UHV) scanning tunnelling microscopy (STM) to study the Ni/W(111) and Ni/Mo(111) systems, it was found that, unlike other deposited metals, nickel is not mor-phologically unstable and therefore little or no reconstruction is observed [18].

Earlier experimental studies on clean iron surfaces have shown that no surface reconstruction is observed on either Fe (110) or (111) surfaces [8]. Surface relaxation of the clean Fe (100) [19], (110) [20] and (111) [21–24] surfaces has been studied experimentally, with contraction of the first interlayer spacing (d_{12}) observed on (100) and (111) and some very little expansion on the (110). Surface relaxation and surface energies of the low Miller indices of iron have also been determined computationally using interatomic potential-based methods [25] and quantum mechanical-based techniques. By employing spin-polarized DFT-GGA methods, Spencer et al. [26] reported the extent of surface relaxation and calculated that the surface energies of Fe increased in the order (100)–(110) < (111). The surface energy of bcc iron is reported to be 2.42 Jm^{-2} , but the specific facet to which this energy corresponds was not stated [27]. Whereas some earlier calculations have shown the (100) surface to be the most stable facet for bcc iron, controversy remains as to the relative stabilities of the (100) and (110) facets of other bcc metal surfaces [28–30]

First principles DFT methods can be successfully employed to investigate monolayer (ML) deposition and the tuning of metal sur-face work functions, as studied earlier for example for Ag and Mo surfaces through the deposition of ultrathin oxide films [31] and the TiN (001) surface through the deposition of Au [32]. In line with these studies, the present work investigates the thermodynamically stable sites for nickel adsorption on to iron and their effect on the extent of surface relaxation, reconstruction and work function of the Fe (100), (110), and (111) surfaces in order to evaluate this procedure as a method to enhance iron surfaces for catalytic reactions, for example for the process of CO_2 activation and reduction.

2. Computational details

All calculations were carried out using spin-polarized calculations based on the density functional theory within the generalized gradient approximation (DFT-GGA), with plane wave basis sets and ultra-soft pseudopotentials, as applied in the Quantum ESPRESSO Package [33], which performs fully self-consistent DFT calculations to solve the Kohn-Sham equations [34]. The Perdew Burke Ernz-erhof (PBE) GGA exchange-correlation functional was employed [35]. The Fermi-surface effects were treated by the smearing technique of Fermi-Dirac, using a smearing parameter of 0.003 Ry. An energy convergence threshold defining self-consistency of the electron density was set to 10^{-6} eV and a beta defining mixing factor for self-consistency of 0.2. The graphics of the atomic structures and the iso-surfaces of the differential electron density plots in this manuscript have been prepared with the XCrysDen software [36].

The various low Miller index surfaces were created from the optimized bulk using the METADISE code [37]. Surfaces were described by the slab model, where periodic boundary conditions are applied to the central super-cell so that it is reproduced periodically throughout space [38]. A vacuum region of 12 Å perpendicular to each surface was tested to be sufficient to avoid interactions between periodic slabs. An energy cut-off of 40 Ry (544 eV) and charge density cut-off of 320 Ry (4354 eV) for the expansion of the plane-wave basis set were sufficient to converge the total energy of the iron systems. The Brillouin zone was sampled using a Monkhorst-Pack [39] k-point mesh of (9 × 9 x 9) for the bulk iron, a mesh of (9 × 9 × 1) for the p(1 × 1) Fe(100), (110) and (111) planes, a mesh of (5 × 9 x 1) for the p(2 × 1) Fe(110) surface and, finally, a mesh of (5 × 5 x 1) for the p(2 × 2) Fe(100) and (111) surfaces. Dif-ferent monolayers were explored including 0.25 ML and 1 ML on all facets, where a ML indicates the ratio of ad-atoms to substrate atoms in the top atomic layer (atoms with the same z coordinate make up a single layer and a full ML being the maximum number of ad-atoms that can be accommodated within a single layer).

3. Results and discussion

3.1. Bulk properties of bcc iron

Iron crystallizes in the bodycentered cubic (bcc) crystal structure and exhibits ferromagnetic behaviour. Our calculated lattice constant and bulk modulus are compared with experimental values in Table 1, where the computed lattice constant of 2.86 Å and bulk modulus of 162.5 GPa, obtained from a fit to the Murnaghan equation of state, show excellent agreement with the experimentally obtained lattice constant of 2.87 Å and bulk modulus of 170 GPa. Non-spin polarized calculations are shown to underestimate the lattice constant, with a predicted value of 2.76 Å, confirming the importance of spin polarization in predicting the lattice constant of bcc Fe. The magnetic moment is computed at 2.43 $_B$, which deviates by <10% from the experimental value of 2.24 $_B$.

The total and projected density of states (DOS) of bcc iron, as shown in Fig. 1, is consistent with metallic behaviour due to avail-able states at the Fermi level, indicating overlap of the conduction and valence bands at the Fermi energy level, with the 3d valence electronic states contributing most to the states at the Fermi level as reported earlier [43]. These consistencies with known experimental results validate the model and input parameters employed in this study.

Table 1
Calculated lattice constant (Å) and Bulk modulus (GPa) of bcc Fe.

Parameter	Non-spin polarised	Spin polarised	Literature
Lattice constant/Å	2.76	2.86	2.87 [31], 2.85 [32]
Bulk modulus/GPa	–	162.5	182.46 [32]
Magnetic moment/ B	–	2.43	2.24 [19], 2.33 [32]
Band gap/eV	–	0.00	0.00 [32]

(Aldén et al., 1994) [29] TB-LMTO.
(Crisan and Crisan, 2011) [41] XRD, SEM and magnetic measurements. (Jain et al., 2013) [42] DFT-GGA with PAW-PP.

Table 2
Calculated unrelaxed and relaxed surface energies (Jm^{-2}) of varying slab thicknesses (atomic layers) of Fe (100), (110) and (111) facets.

Slab thickness	(100)		(110)		(111)	
	Unrelaxed	Relaxed	Unrelaxed	Relaxed	Unrelaxed	Relaxed
2	–	–	2.91	2.71	–	–
3	–	–	2.30	2.30	–	–
4	2.36	2.34	2.29[a]	2.29[a]	3.23	2.82
5	–	–	2.29	2.29	–	–
6	2.28[a]	2.25[a]	2.28	2.28	2.65[a]	2.54[a]
7	–	–	–	–	–	–
8	2.28	2.24	–	–	2.65	2.47

[a] Indicates the various slab thicknesses employed in this study.

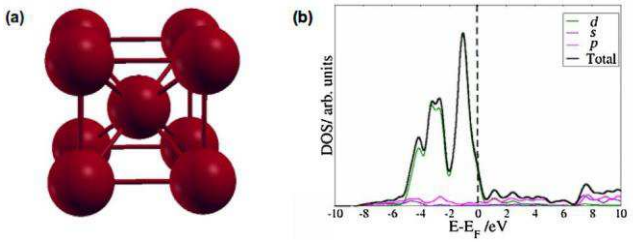

Table 3
Calculated surface energies (Jm^{-2}) with varying numbers of relaxed top atomic layers of the low miller indices of Fe.

Top relaxed layers	(100)	(110)	(111)
1	2.28	2.29	2.65
2	2.28	2.29	2.62
3	2.27	2.29[a]	2.58
4	2.25	–	2.60
5	2.25[a]	–	2.48[a]

[a] Indicates the most stable slab.

3.2. Surface properties

Energy minimizations were carried out on different slab thick-nesses of the Fe (100), Fe (110) and Fe (111) slabs to obtain the appropriate slab thicknesses for the various facets until con-vergence within 1 meV per cell was achieved. Using a p(1 × 1) super-cell and a k-point grid of (9 × 9 x 1), slabs made of four, six and eight atomic layers for the (100) and (111) and two to six atomic layers for the (110) surface were considered. The unrelaxed surface energies (u) of each surface were obtained from a single point cal-culation of the symmetric stoichiometric slabs before relaxation via Eq. (1)

Fig. 1. The bcc structure (a), electronic DOS (total and projected DOS) of bulk Fe.

$$u = \frac{E_{slab}^{unrelaxed} - nE_{bulk}}{2A}$$

where $E_{slab}^{unrelaxed}$ is the energy of the unrelaxed slab, E_{bulk} is the energy of the bulk material, n is the number of bulk units in the surface and A is the surface area of the surface of one side of the slab.

When calculating the relaxed surface energies, following well established convention, we have kept atoms in the last two layers in the bottom side of the slab fixed at their bulk optimised position, relaxing explicitly the atoms in the surface layers only. When only one side of the slab (top) is allowed to relax unconstrainedly, while the atoms at the bottom of the slab are fixed at the bulk positions, the additional energy due to the relaxed surface at the top of the slab must be separated from the energy of the unrelaxed surface at the bottom, as the two differ. Using the unrelaxed surface energy

it is possible to calculate the relaxed surface energy ($_r$) from the total energy of the relaxed slab as:

$$\gamma_r + \gamma_u = \frac{E_{slab}^{relaxed} - nE_{bulk}}{A} \quad (1)$$

where $E_{slab}^{relaxed}$ is the energy of the relaxed slab with the bottom atomic layer(s) frozen.

The computed unrelaxed and relaxed surface energies of the various slab thicknesses are reported in Table 2. From the energies obtained, the relaxed and unrelaxed surface energies indicate that a six atomic layer of the (100) slab, a four atomic layer of the (110) slab and a six atomic layer of the (111) slab are sufficient to model the surface behaviour of these facets.

Having obtained the number of atomic layers that are sufficient to model the different surfaces, we also considered the number of atomic layers that must be fully relaxed in order to converge the surface energies. Table 3 reports the relaxed surface energies for the different numbers of relaxed atomic layers. The surface energy gen-erally decreases slightly for all three surfaces when fewer atomic layers are constrained, although there are fluctuating surface ener-gies in the case of the (111) facet and no change for the (110) surface and a steady decrease in surface energy of the (100) surface. The lowest energy structures are observed when all surface atom layers are relaxed except the bottom layer.

The results in Tables 2 and 3 are summarised diagrammati-cally in Fig. 2. We note that the convergence of the surface energy with respect to slab thickness is the same for both the relaxed and unrelaxed atomic layers for all three facets, and the convergence of energy with respect to layer relaxations is achieved for all sur-faces with a single bottom layer of atoms fixed at their bulk atomic positions. We employed the most stable slabs for subsequent

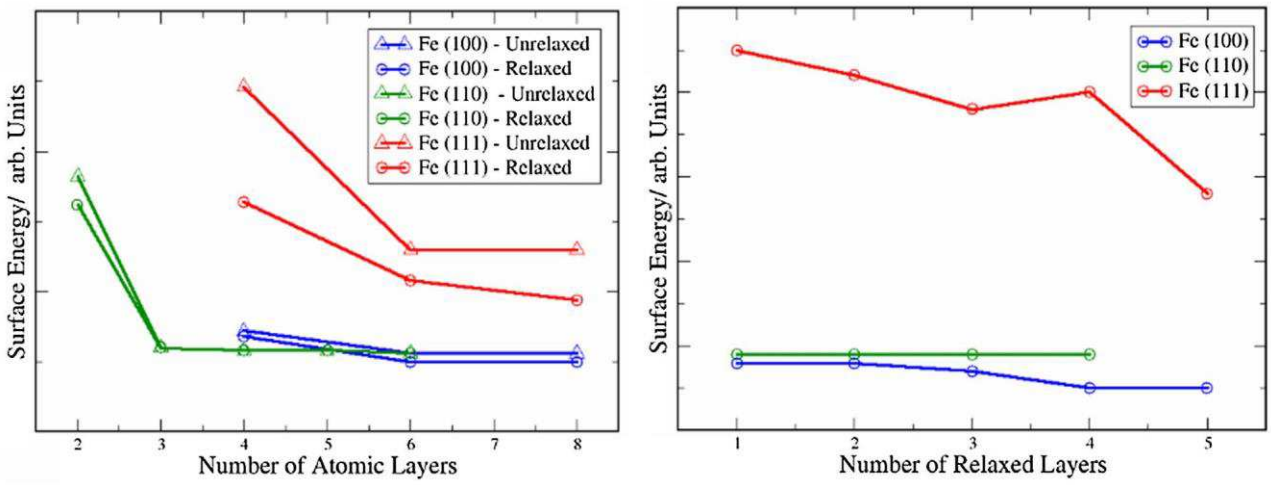

Fig. 2. Surface energy ( ) of Fe low miller index surfaces as a function of the number of atomic layers in the slab (left), and number of surface layers allowed to relax unconstrainedly (right).

Table 4
Comparison of surface energies and magnetic moment from this work with earlier studies.

Surface	This work		Spencer et al. [26]	Alden et al. [29]	Vitos et al. [28]	Tyson et al. [30]	Blonski et al. [43]
	/Jm^{-2}	m/ B	/Jm^{-2}	/Jm^{-2}	/Jm^{-2}	/Jm^{-2}	M/ B
(100)	2.25	2.77	2.29	2.18	2.22	2.42	2.95
(110)	2.29	2.65	2.27	2.66	2.43		2.59
(111)	2.48	2.74	2.52	–	2.73		2.81

(Tyson et al., 1973) [30] theories of crack propagation.
(Aldén et al., 1994) [29] tight binding linear muffin-tin orbitals (TB-LMTO). (Vitos et al., 1998) [28] TB-LMTO.
(Spencer et al., 2002) [26] DFT-GGA (PW91 functional) US-PP.
(Błonski´ and Kiejna, 2007) [43] DFT-GGA PAW-PP.

calculations as indicated in Table 3. A 4-layer slab with three relaxed surface layers was used for the calculations of the (110) surface and a 6-layer slab with five relaxed surface layers for calculations of the (100) and (111) surfaces.

The surface energies reported in Table 4 show decreas-ing stability of (100)–(110) > (111) with surface energies of 2.25–2.29 < 2.48 Jm^{-2} respectively. This trend is in agreement with earlier calculations which report the (100) surface as the most sta-ble surface and the dominant plane expressed in the morphology of the Fe crystal [27–29]. This result also agrees with the work of Spencer et al. [26], who reported a trend of (100)–(110) > (111), with similar energies of 2.29–2.27 < 2.52 Jm^{-2} . The small differ-ences in the calculated surface energies could be attributed to the difference in the functionals employed; Spencer et al. used the PW91 GGA functional whereas we have employed the PBE GGA functional.

The calculated magnetic moment of the bulk ferromagnetic bcc Fe at 2.43 B compared well with experiment (see Table 1) and we also found that the magnetic moment is enhanced on the sur-faces compared to the bulk, where the highest magnetic moment is observed on the (100) and the lowest on the (110) surface, consis-tent with previous studies [43]. The results in Table 4 show that the magnetic moment is calculated to increase from 2.43 B to 2.77 B , 2.65 B and 2.74 B on the (100), (110) and (111) surfaces, respectively.

Using the calculated surface energies, we have obtained the thermodynamic crystal morphology of Fe (Fig. 3) using the Wulff method [44]. The calculated morphology shows the (100) and (110) facets as the predominantly expressed surfaces owing to their low surface energies. Experimental results report a surface energy of 2.42 Jm^{-2} but without identifying any particular surface(s). If this

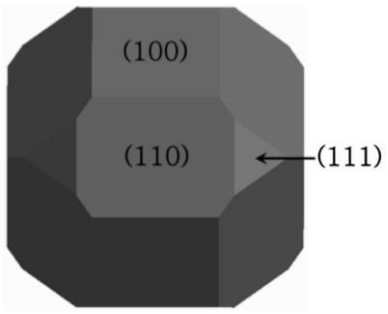

Fig. 3. Thermodynamic equilibrium crystal shape of bcc iron.

value is assumed to be the average of a variety of surface energies for different individual planes, then the average surface energy of the three surfaces calculated in this study at 2.34 Jm^{-2} is approaching the experimental value, especially as we have considered perfect surfaces, whereas defects present on experimental surfaces will alter the surface energy and most likely increase it [45].

We have also characterized the extent of relaxation in the inter-layer spacings of the bare bcc Fe surfaces before Ni deposition and compared them with those obtained from earlier experimental and theoretical studies using the formula:

$$\%\text{Relaxation} = \frac{\text{inter layer spacing (surface)} - \text{inter layer spacing (bulk)}}{\text{inter layer spacing (bulk)}} \times 100 \quad (3)$$

As reported in Table 5, negative/inward relaxation of the surface atoms was found on all three surfaces studied. The atoms in the

Table 5
Surface relaxation (interlayer spacing) of the unreconstructed bare surfaces of iron compared to previous theoretical and experimental studies.

Surface	d_{ij}	Bulk d_{ij} /Å	Relax d_{ij} /Å	Relaxation/%				
				This Work	Literature			
100	d_{12}	1.43	1.39	−2.79	−1.4(±3) [19]	0.35 [25]		−1.89 [26]
	d_{23}	1.43	1.47	2.80		−0.14 [25]		2.59 [26]
	d_{34}	1.43	1.46	2.10				0.21 [26]
	d_{45}	1.43	1.47	2.80				−0.56 [26]
	d_{56}	1.43	1.40	−2.10				−0.14 [26]
110	d_{12}	2.02	2.01	−0.50	0.10(±2) [21]	1(±2) [24]		−0.13 [26]
	d_{23}	2.02	2.04	0.10		0.5(±2) [24]		0.20 [26]
	d_{34}	2.02	2.01	−0.50				−0.06 [26]
111	d_{12}	0.82	0.74	−9.76	−15.4(±3) [22]	−16.9(±3) [23]	−29.7(±7) [24]	−13.3 [26]
	d_{23}	0.82	0.68	−17.07		−9.8(±3) [23]	6.0(±5) [24]	−3.6 [26]
	d_{34}	0.82	0.92	12.20		4.2(±3.6) [23]		13.3 [26]
	d_{45}	0.82	0.68	−17.07		−2.2(±3.6)[23]		−1.2 [26]
	d_{56}	0.82	0.74	−9.76				0.35 [26]

(Legg et al., 1977)[19] Experimental study using low energy electron diffraction (LEED). (Kishi and Itoh, 1996) [25] Theoretical study using Ab-initio molecular dynamics.
(Shih and Jona, 1980) [21] Experimental study using LEED.
(Xu and O'Connor, 1991) [24] Experimental study using Medium Energy Ion Scattering (MEIS). (Shih et al., 1981) [22] Experimental study using LEED.
(Sokolov et al., 1986) [23] Experimental study using LEED and Auger electron Spectroscopy (AES). (Xu and O'connor, 1990) [24] Experimental study using MEIS.
(Spencer et al., 2002) [26] Theoretical study using DFT-GGA.

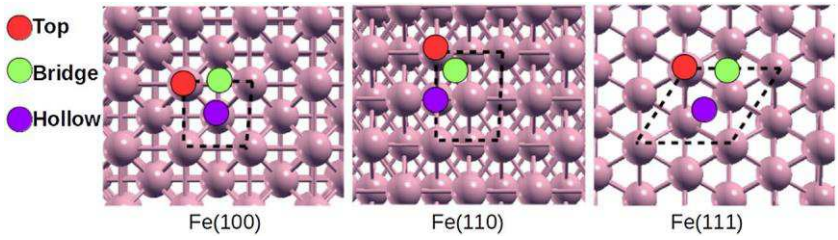

Fig. 4. Top views of the initial adsorption sites on the Fe (100), (110) and (111) surfaces.

topmost layers in particular moved down into the bulk material during energy minimisation, increasing their bonding with sub-surface atoms. This downward movement of the topmost atoms results in a decrease in the first interlayer spacing (d_{12}). The most closed-packed surface, i.e. (110), has the least percentage relaxation of d_{12} , calculated to be <1%. Relaxation was most prominent on the (111) surface, which is also the least stable facet. Our results amplify and are fully compatible with earlier computational and experimental studies of this surface.

3.3. Adsorption of Ni atoms on the Fe surfaces

In order to determine the thermodynamically most stable adsorption site and adsorption geometries, the Ni ad-atom and the topmost atomic layers except the bottom layer of each slab were allowed to relax without constraints until the residual forces on each atom reached 0.01 eV/Å. Symmetry constraints were not imposed on the geometry optimization calculations, and in partic-ular, the Ni ad-atom was free to move away laterally and vertically from the initial adsorption site to find the minimum energy adsorp-tion structure. The three possible adsorption sites investigated on each surface include top, bridge and hollow sites, as shown in Fig. 4.

To characterize the strength of the adsorbate/surface interac-tion, we have calculated the energy of adsorption (E_{ads}) using the formula:

$$E_{ads} = E_{surf+Ni} - (E_{surf} + E_{Ni}) \quad (4)$$

where $E_{surf+Ni}$ represents the total energy of the adsor-bate/substrate (Ni/Fe) system, E_{surf} is the energy of bare surface and E_{Ni} is the energy of a Ni atom. Thus, a negative adsorption energy indicates an exothermic and favourable adsorption process.

The adsorption energies E_{ads} were calculated in two ways i.e. $E_{ads(Ni\text{-}B)}$ which is the adsorption energy calculated with reference to nickel atom of a bulk nickel material (where E_{Ni} is the energy per bulk Ni atom) and $E_{ads(Ni\text{-}A)}$ is the adsorption energy calculated with reference to atomic nickel in its free or gaseous state (where E_{Ni} is energy of Ni atom in vacuum) as indicated in Table 6.

On the (100) facet, a single nickel atom is adsorbed onto a p(1 × 1) cell which represents a 1 ML and total coverage of the surface. On computing the starting structures for the Ni/Fe (100) system, two possible sites were obtained as compiled in Table 6. The top adsorption site was obtained as a stable configuration, but both the bridge and hollow initial sites converged to the Ni ad-atom being located at the hollow site. The Ni ad-atom is pref-erentially adsorbed on the surface hollow site with a five-fold coordination, releasing an adsorption energy of 26.6 $kJmol^{-1}$ upon nickel deposition from the bulk material. Adsorption of a nickel atom from vacuum to the hollow site is more exothermic, releas-ing an energy of 483.1 $kJmol^{-1}$. At the less preferred top site on the (100) facet, however, nickel is more stable in its bulk than at this adsorption site, with an endothermic adsorption energy of 109.4 $kJmol^{-1}$. However, deposition of nickel from its vapourised state still leads to a favourable adsorption with an adsorption energy of −347.1 $kJmol^{-1}$. The surface interlayer spacing ($d_{(Fe\text{-}Ni)}$), when nickel is adsorbed on the hollow site is smaller, i.e. 1.31 Å compared to 2.20 Å at the top site, which shows a higher Fe-Ni interaction at the preferred site, resulting in a higher adsorption energy at the hollow site. At the top site, Ni coordinates to one

Table 6
Adsorption energies, interatomic distances and coordination numbers of Ni ad-atom on the (100), (110) and (111) surfaces of Fe at >0.25 ML.

Surface	Coverage	Ads-site	E_{ads} (Ni-B)/kJmol^{-1}	E_{ads} (Ni-A)/kJmol^{-1}	$d_{(Fe-Ni)}$/Å	Fe-Ni/Å	Ni-Ni/Å	
Fe (100)	1 ML	Top	109.4	−347.1	2.20	2.20	2.86	1
		Hollow	−26.6	−483.1	1.31	2.40	2.86	5
Fe (110)	1 ML	Top	27.4	−429.0	2.24	2.24	2.47	1
	0.5 ML	Top	77.9	−378.5	2.24	2.24	3.45	1
		Hollow	52.1	−404.3	1.08	1.94	3.45	4
Fe (111)	1 ML	Top	222.4	−234.0	2.14	2.14	4.0	1
		Bridge	57.0	−399.5	1.08	2.20	4.0	3
		Hollow	−37.4	−493.9	0.65	2.32	4.0	7
	2 ML	Top	24.9	−431.6	0.56	1.99	2.46	1
		Bridge	−24.2	−480.7	0.56	1.99	2.46	5
	3 ML	Top	−15.2	−471.6	0.90	1.99	2.43	1

Where **Ads-site** is the converged nickel sites from top, bridge and hollow initial guess sites, $\mathbf{E_{ads}}$ **(Ni-B)** is the adsorption energy calculated with reference to bulk nickel atom, $\mathbf{E_{ads}}$ **(Ni-A)** is the adsorption energy calculated with reference to gaseous nickel atom, $\mathbf{d}_{(Fe-Ni)}$ is the top iron and nickel interlayer spacing, **Fe-Ni** is the interatomic distance between iron and the closest nickel atom, **Ni-Ni** is the interatomic distance between neighbouring nickel atoms and shows the number of Fe atoms coordinated to one Ni ad-atom.

iron atom with an interatomic distance of 2.20 Å and at the hol-low site. Ni coordinates to five iron atoms where the smallest Fe-Ni inter-nuclear distance is 2.40 Å. The top site is clearly a metastable configuration.

Within a p(1 × 1) cell, two nickel ad-atoms were introduced onto the (110) facet, which corresponds to a 1 ML adsorption coverage. Three distinct initial guess sites were considered as in the case of the other facets i.e. top, bridge and hollow. All the initial sites con-verged to the top site with an endothermic binding energy per atom of 27.4 kJmol^{-1} with respect to the bulk nickel atom and an exother-mic adsorption process with adsorption energy of −430.8 kJmol^{-1} when Ni is adsorbed from its gaseous state, indicating the top site as the preferred adsorption site on the most close-packed Fe (110) surface.

When the coverage is reduced to 0.5 ML, where one Ni ad-atom is adsorbed on the p(1 × 1) cell at the top, bridge and hollow sites, the preferred adsorption site is observed as the hollow site with a less favourable adsorption energy (52.1 kJmol^{-1} from the bulk and −404.3 kJmol^{-1} from vacuum). Both the bridge and hollow initial Ni ad-atom sites converged to the hollow site. The Fe-Ni interaction is increased at the hollow site compared to the top site, characterised by the reduced Fe-Ni interlayer distance ($d_{(Fe-Ni)}$), from 2.24 Å at the top site to 1.08 Å at the hollow site and increased adsorption energy which quantitatively show stronger binding.

The change in the preferred adsorption site from hollow to top site on the (110) surface at increased coverage of 1 ML could be attributed to surface crowding and reduced substrate-adsorbate interaction. A change in preferred adsorption site is not observed on the other facets at 1 ML coverage, because of the high surface atomic density on the (110) surface, which is the closest packed face of iron surfaces explored. This behaviour on the Fe(110) has been reported before by Jiang and Carter [48], who reported the bridge site for CO adsorption at 0.25 ML coverage, but upon increasing CO coverage to 0.5 ML, they observed that due to surface crowding the adsorption site changed to the top site.

We suspect that at 1 ML coverage on the (110) facet, there is an evolution in the film structure which is mostly observed as monolayer transitions to multilayers in film growth, whereby with increasing film thickness the ad-atoms assume their bulk structure [9]. The monolayer film is reported experimentally to be pseudo-morphic [16] (i.e. the nickel takes the exact position of iron in the top layer) at 1 ML deposition coverage, but at higher cover-ages above 1 ML, the structure changes into the close-packed fcc (111) face of nickel with bulk inter-nuclear distances [14]. We observed the pseudo-morphic crystal structure at 1 ML coverage, but below 1 ML, i.e. 0.5 ML, the ad-atom is at a more stable and higher-coordinated hollow site, thereby forming a stepped surface only below the 1 ML coverage.

Apart from the observation of a pseudo-morphic layer at first monolayer coverage of nickel on tungsten [10,16], Schmidthals et al. [14], used STM to observe three different structural evolutions before the completion of the first monolayer, i.e. a pseudo-mophic layer below 0.2 ML, as well as (8 × 1) and (7 × 1) distorted struc-tures before the formation of fcc (111) above 1 ML. These studies, including ours, support the possible movement of the nickel ad-atoms, nickel from the hollow site moves towards the top site at 0.5 ML coverage and finally relocates to the top site to form a nickel pseudo-morphic film in the first monolayer regime.

Using a p(1 × 1) cell of the stepped (111) surface, adsorption of one nickel ad-atom corresponds to 1 ML coverage. Again, the preferred adsorption site is identified after optimisation to be the hollow site with a seven-fold coordination and an exothermic adsorption energy of −37.4 kJmol^{-1} when nickel is adsorbed from its solid state and −493.9 kJmol^{-1} from its gaseous state. The top 3 layers of the stepped (111) surface are exposed on the surface, and hence the surface coverage was increased from 1 ML to 3 ML (i.e. total surface coverage). At 2 ML coverage, we adsorbed one more nickel atom to the optimised 1 ML covered (111) slab at two initial sites, namely the two possible available vacant sites, i.e. the top and bridge sites since all the hollow sites are already occupied, in order to explore the stability of these sites. After optimisation, the bridge site is found to be the preferred site for the second Ni ad-atom. At this site, adsorption is exothermic with an adsorption energy per atom of −24.2 kJmol^{-1} with respect to the bulk nickel atom and −480.7 kJmol^{-1} with respect to the vapourised nickel atom. The 2 ML coverage of the (111) surface is as expected less favourable compared to the 1 ML coverage.

At 3 ML coverage, a third nickel atom is introduced to the optimised 2 ML covered slab at the only available top site. The adsorption energy per atom is further reduced at 3 ML coverage, where a less exothermic adsorption energy of −15.2 kJmol^{-1} and −471.6 kJmol^{-1} is calculated with reference to bulk nickel and gaseous nickel, respectively. Therefore on the (111) facet, as more nickel ad-atoms interact with the surface, the energetics of adsorp-tion become less favourable.

Adsorption is favourable with reference to the bulk nickel atom on the (100) and (111) at the preferred hollow sites, but not on the (110) facet which suggests that nickel atoms are more stable in the bulk Ni metal than when deposited on the (110) facet. The lattice constant of iron is about 2.86 Å, while that of nickel is about 3.52 Å, which could contribute to the high affinity of nickel to bind to the more open surfaces of iron. The adsorption of the vapourised nickel atom is, however, exothermic on all sites of the three surfaces,

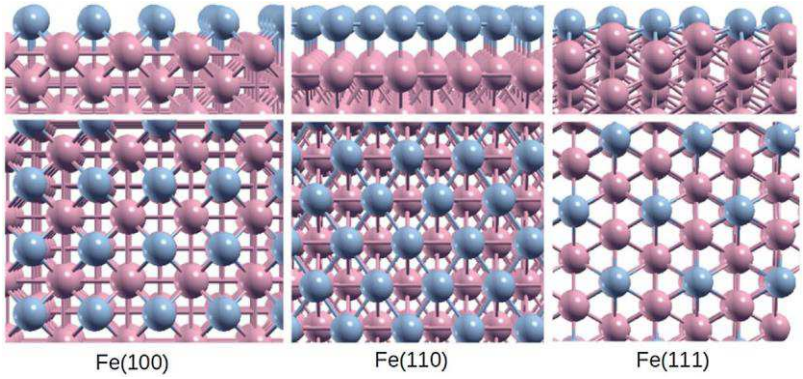

Fig. 5. Side (top) and top (bottom) views of the preferred 5-fold, top and bottom 10-fold surface sites on the Fe (100), (110) and (111) surfaces respectively at 1 ML coverage.

showing that, as expected, deposition is favoured from the vapour phase. Comparing the lowest energy sites of the Fe-Ni systems at 1 ML (see Fig. 5), we find that the strength of adsorption decreases in the order (111) [−37.4 kJmol^{-1} /−493.9 kJmol^{-1}] > (100) [−26.6 kJmol^{-1} /−483.1 kJmol^{-1}] > (110) [27.4 kJmol^{-1} /−429.0 kJmol^{-1}]. This binding energy trend is consistent with the extent of Fe-Ni layer separation ($d_{Fe\text{-}Ni}$), which decreases in the same order (i.e. increasing Fe-Ni distances) of

Table 7
Adsorption energies, interatomic distances and coordination numbers of Ni ad-atom on the (100), (110) and (111) surfaces of Fe at 0.25 ML coverage.

Surface	Ads-site	E_{ads} (Ni-B)/kJmol^{-1}	E_{ads} (Ni-A)/kJmol^{-1}	$d_{(Fe\text{-}Ni)}$/Å	Fe-Ni/Å	Ni-Ni/Å	
Fe (100)	Top	144.7	−313.5	2.11	2.11	5.71	1
	Hollow	−18.8	−475.2	1.30	2.42	5.71	5
Fe (110)	Top	108.6	−347.8	2.30	2.30	5.71,4.04	1
	Hollow	66.7	−389.7	1.78	2.24	5.71,4.04	4
Fe (111)	Top	236.2	−221.9	2.13	2.13	8.08	1
	Hollow	−38.7	−496.8	0.64	2.29	8.08	7

Table 8
Surface relaxations of unreconstructed nickel-deposited surfaces.

Surface	Coverage/ML	Spacing	Bare Surface/Å	Ni-deposited Surface/Å	Relaxation/%
(100)	0.25	d_{12}	1.39	1.41	1.44
		d_{23}	1.47	1.47	0.00
		d_{34}	1.46	1.45	−0.68
	1	d_{12}	1.39	1.47	5.76
		d_{23}	1.47	1.47	0.00
		d_{34}	1.46	1.45	−0.68
		d_{45}	1.47	1.46	−0.68
		d_{56}	1.40	1.37	−2.14
(110)	0.25	d_{12}	2.01	2.04	1.49
		d_{23}	2.04	2.04	0.00
		d_{34}	2.01	2.01	0.00
	0.5	d_{12}	2.01	2.01	0.00
		d_{23}	2.04	2.04	0.00
		d_{34}	2.01	2.01	0.00
	1	d_{12}	2.01	2.05	1.99
		d_{23}	2.04	2.03	−0.49
		d_{34}	2.01	2.01	0.00
(111)	0.25	d_{12}	0.74	0.75	1.35
		d_{23}	0.68	0.73	7.35
		d_{34}	0.92	0.89	−3.26
	1	d_{12}	0.74	0.79	6.76
		d_{23}	0.68	0.89	30.88
		d_{34}	0.92	0.91	−1.09
		d_{45}	0.68	0.65	−4.41
		d_{56}	0.74	0.82	10.81
	2	d_{12}	0.74	0.98	32.43
		d_{23}	0.68	0.85	25.00
		d_{34}	0.92	0.88	−4.35
		d_{45}	0.68	0.68	0.00
		d_{56}	0.74	0.82	10.81
	3	d_{12}	0.74	0.83	12.16
		d_{23}	0.68	0.80	17.65
		d_{34}	0.92	0.93	1.09
		d_{45}	0.68	0.68	0.00
		d_{56}	0.74	0.78	5.41

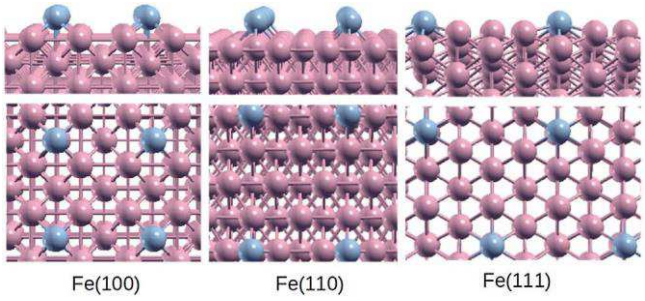

Fig. 6a. Side (top) and top (bottom) views of the preferred 5-fold, top and bottom 10-fold surface sites on the Fe (100), (110) and (111) surfaces respectively at 0.25 ML coverage.

(111) [0.65 Å] < (100) [1.31 Å] < (110) [2.24 Å], whereas the Ni-Ni interaction increases in the same order (decreasing Ni-Ni dis-tances) at (111) 4.0 Å > (100) 2.86 Å > (110) 2.47 Å. The weaker the Ni-Ni interaction, the stronger the Fe-Ni interaction and the more favoured the adsorption, as is for example clearly observed on the (111) facet.

Using a p(2 × 2) super-cell for the (100) and (111) facets and a p(2 × 1) super-cell for the (110) facet, where all atomic layers except the top three layers were kept at their bulk positions, we further studied nickel adsorption at a lower surface coverage of 0.25 ML on all three surfaces. One nickel atom was adsorbed on three distinct sites i.e. the top, bridge and hollow surface sites of each facet as shown in Fig. 4.

The most preferred sites are the hollow sites for all three surfaces as shown in Fig. 6a and Table 7. At the hollow site, nickel is in a five-fold coordination on the (100) surface, four-fold coordination on the (110) surface and seven-fold coordination on the (111) surface, as already seen previously at 1 ML coverage of the (100) and (111) facets and 0.5 ML coverage on the (110) facet.

Adsorption energies at 0.25 ML coverage show the same trend as the 1 ML covered surfaces i.e. (111) > (100) > (110), where the most favoured adsorption occurs on the (111) facet with an exothermic adsorption energy (-38.7 kJmol^{-1}) for nickel deposition from its bulk and a more exothermic energy (-496.8 kJmol^{-1}) for gaseous nickel deposition. On the (100) surface adsorption energies of -18.8 kJmol^{-1} and -475.2 kJmol^{-1} are obtained when nickel is deposited from the bulk material or vacuum respectively. The least favoured and endothermic adsorption is still observed on the (110) facet at 0.25 ML coverage, where an energy of 66.7 kJmol^{-1} is required to deposit nickel from the solid phase, but 389.7 kJmol^{-1} is released upon deposition from the gaseous nickel state. The Fe-Ni interaction trend of (111) [0.64 Å] > (100) [1.30 Å] > (110) [1.78 Å] from its Fe-Ni interlayer distance ($d_{(Fe-Ni)}$) still remains the same as observed at 1 ML coverage.

3.4. Relaxations of unreconstructed Ni-doped Fe surfaces

Nickel deposition induces relaxation of all three surface orienta-tions but no reconstruction. Positive interlayer spacing relaxations indicate surface expansions, while contractions are denoted by negative interlayer spacing (see Table 8). Expansion of the first interlayer spacing (d_{12}) of the iron is generally observed on depo-sition of Ni on all facets due to bond formation between the deposited Ni and the iron surfaces. This behaviour is also charac-terised by the increased relaxation with higher adsorption energy i.e. (111) > (100) > (110) as a result of stronger bond formations, which results in bond weakening within the slabs.

At 0.25 ML, the (100) surface relaxation ranges between −0.68 to 1.45% which increases to between −2.14 to 5.78% at 1 ML. Apart from normal displacement of the (100) surface atoms, the atomic layers are found to displace laterally by shifting in both x and y direction by the same amount (see Table 9) to increase the slab stability as shown in Fig. 5.

Table 9
Extent of lateral displacement on the (100) facet in both x and y axis.

Bare Space/Å	Deposited Space/Å	Relaxation/%
1.43	1.38	−3.50
2.86	2.81	−3.50
1.43	1.39	−2.80
2.86	2.83	−1.05
1.43	1.41	−1.40

At 0.25 ML coverage, the (110) surface relaxes the least com-pared with the other two surfaces, between 0–1.49% which increases at 1 ML coverage to between −0.49 and 1.99%. The slab is, however, preserved at 0.5 ML coverage where the surface is most likely to be saturated at the preferred 4-fold site. DFT-GGA calcu-lations have shown that the deposited nickel film on W(110) was more strained at pseudo-morphic 1 ML coverage than in the (1 × 7) configuration (equivalent to about 1.23 ML) [18]. The large strain leads to more enhanced relaxations of the sub-atomic layer at 1 ML surface coverage [16]. In our DFT calculations, this phenomenon of enhanced relaxation is also observed at 1 ML coverage, whereby the nickel film is forced to form a pseudo-morphic structure at the top site, experiencing strain, from the preferred hollow site at the nucleation/isolated stages. The strain on the nickel film leads to enhanced sub-monolayer relaxation.

Finally, the (111) surface relaxes the most compared to the other two surfaces, as expected, due to its stronger nickel binding and least stability. A relaxation of between −3.26 to 7.35% is observed on the (111) surface at 0.25 ML deposition, which increases to between −4.41 to 30.88% at 1 ML coverage. At 2 ML coverage, surface relax-ation of the (111) surface is enhanced to within the range of −4.35 to 32.43%, while at 3 ML the extent of relaxation is reduced below that of the 1 ML deposited (111) slab to between 0–17.65%.

As a result of surface saturation, there is crowding and weaker Fe-Ni interactions as more nickel layers are introduced, resulting in an increased interlayer distance $d_{(Fe-Ni)}$ from 0.65 Å at 1 ML to 0.90 Å at 3 ML, while there is a decreased interlayer distance $d_{(Fe-Ni)}$ at 2 ML from 0.65 ML at 1 ML to 0.56 Å (see Table 8).

3.5. Electronic properties of nickel deposited surfaces

We now discuss the electronic properties of the bare and nickel-deposited Fe (100), (110) and (111) surfaces. Analyses of the projected density of states (PDOS) help us to gain insight into the nature of the bonding of the nickel ad-atom layers on the various iron surfaces. We have calculated the electronic density of states (DOS) projected on the 3d orbitals of the interacting iron and nickel at 1 ML coverage for the (100), (110) and (111) surfaces. As shown in Fig. 6b, upon deposition of the nickel layer, the splitting and broadening of peaks show electron transfer, strong interaction and chemical bonding between the nickel and the surface iron atoms. Nickel adsorption on the three facets is shown to be a chemisorbed process.

Further insight into the nature of the interaction and charge distribution between the nickel layers and iron surfaces can be obtained from the isosurfaces of the induced charge density (p) plot, which was calculated using the equation:

$$(\rho) = (\rho_{Fe+Ni}) - (\rho_{Fe} + \rho_{Ni}) \quad (5)$$

where (ρ_{Fe+Ni}) is the charge density of the deposited system, ρ_{Fe} is the charge density of the bare surface, and ρ_{Ni} is the charge density of the isolated nickel ad-atom. Fig. 7 shows that there is signifi-cant charge transfer between the nickel layer and Fe layers in the

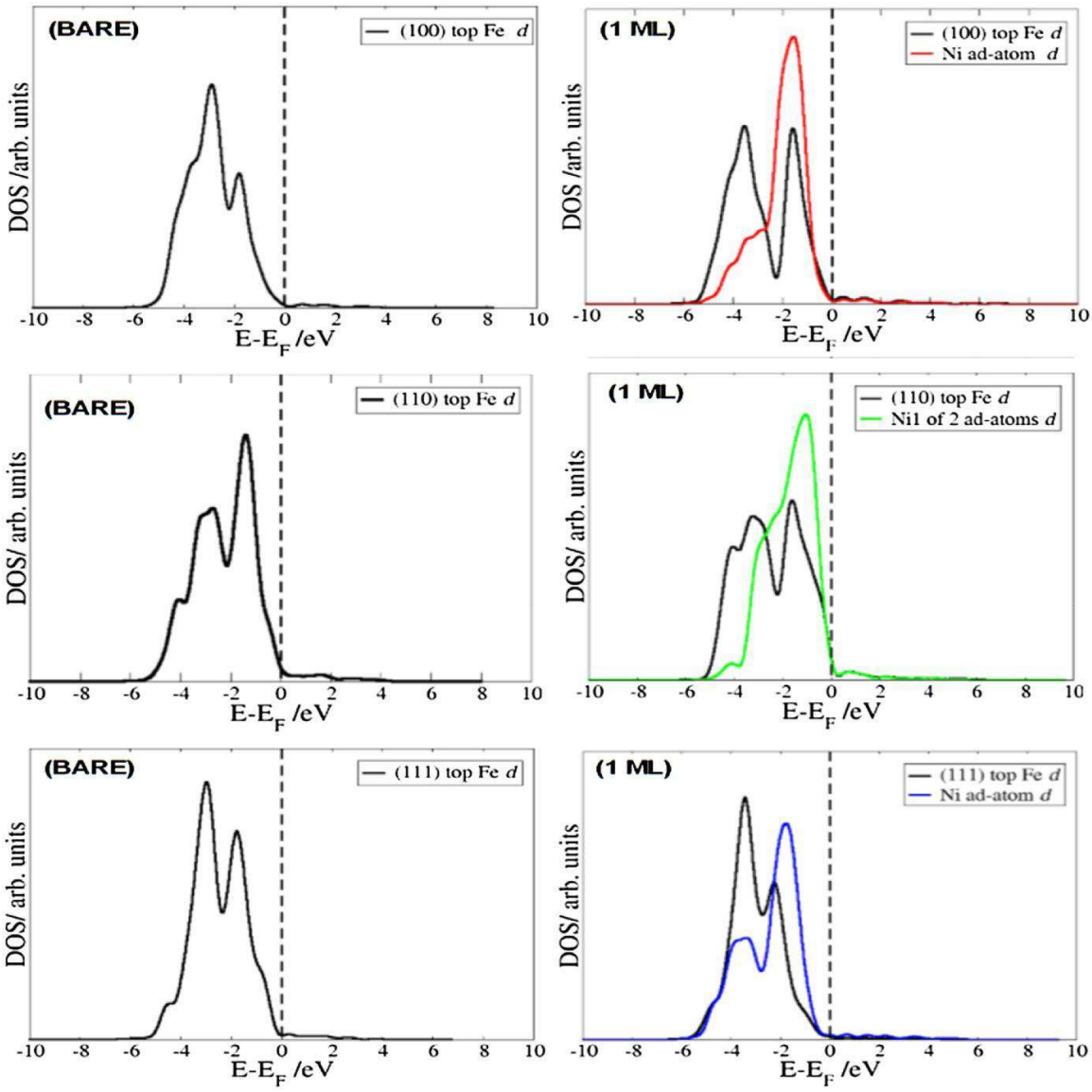

Fig. 6b. Projected density of state plots for bare and deposited (100), (110) and (111) surfaces.

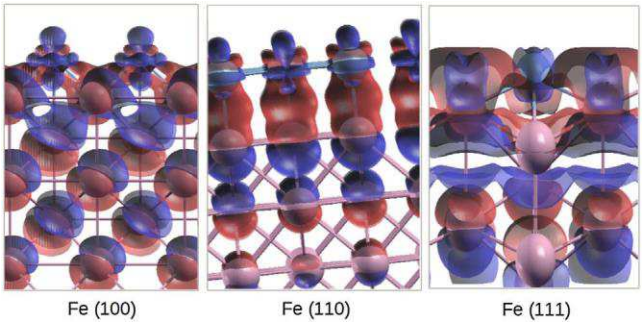

Fig. 7. The charge density difference contour plot which shows the interaction of the Ni ad-atoms with the Fe (100), Fe (110) and Fe (111) surfaces. The blue contours indicate electron density increase (gain) by 0.05 electrons/Å^3 and red contours indi-cate electron density decrease (depletion) by 0.05 electrons/Å^3 . (For interpretation of the references to color in this figure legend, the reader is referred to the web version of this article.)

slabs with electron accumulation on the nickel and rearrangement within the iron slabs, showing strong Fe-Ni interactions and chem-ical bonding which is particularly evident on the (111) surface. We next computed the work function (˚) of the iron surfaces before and after the deposition of the nickel layer. The work function is calculated as the difference between the electrostatic potential in the vacuum region and the Fermi energy as:

$$^{\circ} = V_{vac} - E_F \quad (6)$$

where V_{vac} is the vacuum electrostatic potential, and E_F is the Fermi level energy. We obtained a trend of (110) > (100)–(111) in the work function for the bare surfaces with calculated values of 4.76 eV, 3.80 eV and 3.84 eV respectively (see Table 10), which shows ade-quate agreement with experimentally [29] determined values of 4.50 eV for the (100) surface, and 5.21 eV for the (110) surface, par-ticularly in the relative trend. Our predicted work function for the Fe (100) in particular shows excellent agreement with an earlier DFT-GGA calculation by Cao [30] who also obtained a work function of 3.80 eV for the (100) surface. Błonski´ and Kiejna, using DFT-GGA spin polarised methods, also reported the same work function trend as (110) > (111) > (100) for bare iron surfaces using Ultra-soft [45] and Projector-augmented-wave [43] pseudopotentials. These results seem to suggest that DFT-GGA functionals clearly

Table 10
Work function change at preferred sites at various nickel surface coverages.

Surface	Condition	/eV		
		This work	Diff	Literature
(100)	Bare	3.80	–	4.50 [19], 3.80 [30], 3.86 [35], 3.91 [33]
	0.25 ML-Ni	4.04	0.24	–
	1 ML-Ni	4.29	0.49	–
(110)	Bare	4.76	–	5.21 [19], 4.81 [36], 4.76 [33]
	0.25 ML-Ni	4.59	−0.17	–
	0.5 ML-Ni	4.60	−0.16	–
	1 ML-Ni	4.72	−0.04	–
(111)	Bare	3.84	–	3.95 [36], 3.90 [33]
	0.25 ML-Ni	4.05	0.21	–
	1 ML-Ni	4.17	0.33	–
	2 ML-Ni	4.24	0.40	–
	3 ML-Ni	4.28	0.44	–

(Aldén et al., 1994) [19] Experimental.
(Cao, 2009) [30] DFT-GGA.
(Błonski´ and Kiejna, 2004) [36] DFT-GGA.
(Błonski´ and Kiejna, 2007) [33] DFT-GGA.

underestimate the work function by between 0.5–0.7 eV when compared to the experimental results.

Upon deposition, as shown in Table 10, at 0.25 ML the work function increases by 0.24 eV to 4.04 eV on Fe (100). When the cov-erage is increased to 1 ML the work function is further increased to 4.29 eV. On the (111) facet at 0.25 ML the work function is increased by 0.21 eV to 4.05 eV upon Ni deposition and it also increases as more nickel layers are adsorbed onto the surface, with the work function further increasing to 4.17 eV, 4.24 eV and 4.28 eV at 1 ML, 2 ML and 3 ML coverages, respectively, i.e. by 0.33 eV, 0.40 eV and 0.44 eV in the same order. The work function, however, decreases on the (110) facet on deposition of nickel. At 0.5 ML deposition, the work function has decreased from 4.76 to 4.60 eV and at 0.25 ML it has decreased to 4.59 eV. Finally, at 1ML coverage on the Fe (110), the reduction in the work function is minimal, by only 0.04 eV from 4.76 eV to 4.72 eV. Ni deposition at < 1 ML on the (110) facet changes both the surface composition and the highly dense (stable) sur-face topology to a more open stepped surface (less stable), which generally have better reactivity than their flat counterparts [47].

The drastic change in work function observed on the (110) facet at 1 ML coverage from the 0.5 ML coverage also confirm the change in surface roughness, i.e. decreasing from 0.04 eV, to 0.16 eV and 0.17 eV at 1 ML, 0.5 ML and 0.25 ML coverages, respectively, as seen experimentally upon nickel deposition on the W(110) surface [10]. Where the initial work function dips below 1 ML coverage due to surface roughness, it rises steeply at 1 ML coverage.

Deposition reduces the work function on the most stable and predominant (110) surface, but increases it on the (100) and (111) surfaces, increasingly so as more layers of nickel are deposited. Our results show that monolayer nickel deposition on the (110) surface of iron increases its electrochemical reactivity which has impor-tant implications for its use as a more efficient cathode material for processes such as CO_2 reduction and H_2 O splitting to produce clean fuels. The more open (100) and (111) surfaces with lower and similar work functions are passivated at monolayer deposition of nickel towards electrochemical reactions. Passivation of these facets is, however, advantageous for the steel industry for exam-ple, since the (100) and (111) monolayer deposited surfaces would be less susceptible to corrosion.

4. Conclusions

Our spin-polarised DFT-GGA calculation results reveal that deposition of nickel monolayers on the Fe (100), (110) and (111) surfaces is preferred at the hollow sites at 0.25 ML and 1 ML coverages, although deposition is most favourable at the top site at 1 ML coverage on the most close-packed (110) facet. Gener-ally, Ni binds more strongly at the more open surfaces and binds least on the densely packed surface, where we observed the trend (111) < (100) < (110) for Fe-Ni interface separations, from the mea-sured Fe-Ni interlayer spacings ($d_{Fe\text{-}Ni}$). Deposition induces surface relaxation of the facets but no reconstruction and the extent of relaxation increases with increasing Fe-Ni interactions, due to the topology of the faces and increasing Ni coverage. The (100) and (111) facets are passivated by deposition, as the work function is higher than the pure Fe surface and increases with increasing Ni coverage. The raised work function implies less electrochemical reactivity and suppressed surface oxidation (with a lower corrosion tendency) as a consequence of Ni monolayer deposition. Although the (110) surface topology does not favour nickel deposition com-pared to the other surfaces, deposition leads to surface activation with a decreased surface work function. Since the (110) facet is the most stable and predominant facet in iron crystal particles, the increased reactivity of the Ni-deposited (110) surface, especially at 0.25 ML coverage, may show enhanced electro-catalytic appli-cability, compared to the clean (110) surface, for example in CO_2 activation and reduction processes. The results suggest that nickel deposition on the (110) surface of Fe enhances its potential for electro-catalysis, while deposition on the (100) and (111) improves their corrosion-resistant properties.

Acknowledgements

The authors gratefully acknowledge the UK's Royal Society and Leverhulme Trust for a research grant under the Royal Society-Leverhulme Africa Award Scheme. E.A., R.T. and C.R.K. also acknowledge the National Council for Tertiary Education, Ghana, for a TALIF research grant.

References

[1] W. Gong, B. Hao, Z. Wei, D.J. Ferguson, T. Tallant, J.A. Krzycki, M.K. Chan, Structure of the alpha2epsilon2 Ni-dependent CO dehydrogenase component of the methanosarcina barkeri acetyl-CoA decarbonylase/synthase complex, Proc. Natl. Acad. Sci. U. S. A. 105 (2008) 9558–9563.

[2] J.-H. Jeoung, H. Dobbek, Carbon dioxide activation at the Ni,Fe-cluster of anaerobic carbon monoxide dehydrogenase, Science (New York, N. Y.) 318 (2007) 1461–1464.

[3] J. Nerlov, S. Sckerl, J. Wambach, I. Chorkendorff, Methanol synthesis from CO_2 CO and H_2 over cu (100) and Cu (100) modified by Ni and Co, Appl. Catal. A Gen. 191 (2000) 97–109.

[4] G.A. Somorjai, Y. Li, Introduction to Surface Chemistry and Catalysis (Wiley, Hoboken, NJ) 2nd Ed. (2010).

[5] G. Somorjai, U. Starke, Monolayer surface structure analysis, Pure Appl. Chem. 64 (1992) 509–527.
[6] H. Shih, F. Jona, D. Jepsen, P. Marcus, Metal-surface reconstruction induced by adsorbate: Fe(110) p(2 × 2)-S, Phys. Rev. Lett. 46 (1981) 731–734.
[7] E. Bauer, Growth of thin films, J. Phys. Condens. Matter 11 (1999) 9365–9385.
[8] K. Yoshida, G.A. Somorjai, The chemisorption of CO, CO_2 , C_2H_2 , C_2H_4 , H_2 and NH_3 on the clean Fe(100) and (111) crystal surfaces, Surf. Sci. 75 (1978) 46–60.
[9] J.H. van der Merwe, E. Bauer, Structure and growth of crystalline superlattices: from monolayer to superlattices, Phys. Rev. B 49 (1994) 2127–2137.
[10] J. Kolaczkiewicz, E. Bauer, The adsorption of Ni on W(110) and (211) surfaces, Surf. Sci. 144 (1984) 495–511.
[11] K.P. Kaemper, W. Schmidt, G. Guentherodt, H. Kuhlenbeck, Thickness dependence of the electronic structure of ultrathin, epitaxyl Ni (111)/W(110) layers, Phys. Rev. B 38 (1988) 9451.
[12] C. Koziol, G. Lilienkamp, E. Bauer, Electronic properties of ultrathin nickel films on W(110), Phys. Rev. B 41 (1990) 3364.
[13] X. Mingde, R.J. Smith, Growth of thin nickel films on W (110), J. Vac. Sci. Technol. A 9 (1991) 1828.
[14] C. Schmidthals, D. Sander, A. Enders, J. Kirschner, Structure and morphology of Ni monolayers on W(110), Surf. Sci. 417 (1998) 361–371.
[15] M. Tikhov, E. Bauer, Growth, structure and energetics of ultrathin ferromagnetic single crystal films on Mo (110), Surf. Sci. 232 (1990) 73–91.
[16] P.J. Berlowitz, D.W. Goodman, CO methanation and ethane hydrogenolysis over Ni thin films supported on W(110) and W(100), Surf. Sci. 187 (1987) 463.
[17] T.E. Madey, J. Guan, C.H. Nien, C.-H. Dong, H.-S. Tao, R.A. Campbell, Faceting induced by ultrathin metal films on W(111) and Mo(111): structure, reactivity and electronic properties, Surf. Rev. Lett. 3 (1996) 1315.
[18] N. Stojic, N. Binggeli, Surface stress of Ni adlayers on W(110) the critical role of the surface atomic structure, J. Phys. Condens. Matter 24 (2012) 13.
[19] K. Legg, F. Jona, D. Jepsen, P. Marcus, Low-energy electron diffraction analysis of clean Fe (001), J. Phys. C 10 (1977) 937.
[20] C. Xu, D.J. O'Connor, Surface structure and segregation of Fe0.72Cr0.28(110), Nucl. Instrum. Methods Phys. Res. Sect. B 53 (3) (1991) 326–331.
[21] H. Shih, F. Jona, The atomic structure of Fe (110), J. Phys. C. Solid State Phys. (1980) 3801.
[22] H. Shih, F. Jona, D. Jepsen, P. Marcus, Atomic structure of Fe *{*111*}*, Surf. Sci. 104 (1981) 39–46.
[23] J. Sokolov, F. Jona, P. Marcus, Multilayer relaxation of a clean bcc Fe*{*111*}* surface, Phys. Rev. B Condens. Matter 33 (1986) 1397–1400.
[24] C. Xu, D.J. O'connor, Fe(111) surface relaxation analysis by in- and out-of-plane MEIS, Nucl. Instrum. Methods Phys. Res. Sect. B 51 (1990) 278–282.
[25] T. Kishi, S. Itoh, Surface relaxation of Fe(001) by ab initio molecular dynamics, Surf. Sci. 357 (1996) 186–189.
[26] M.J. Spencer, A. Hung, I.K. Snook, I. Yarovsky, Density functional theory study of the relaxation and energy of iron surfaces, Surf. Sci. 513 (2002) 389–398.
[27] W.R. Tyson, W.A. Miller, Surface free energies of solid metals: estimation from liquid surface tension measurements, Surf. Sci. 62 (1977) 267–276.
[28] L. Vitos, A.V. Ruban, H.L. Skriver, J. Kolla, The surface energy of metal, Surf. Sci. 411 (1998) 186–202.
[29] M. Aldén, H. Skriver, S. Mirbt, B. Johansson, Surface energy and magnetism of the 3d metals, Surf. Sci. 94 (1994) 4028.
[30] W. Tyson, R. Ayres, D. Stein, Anisotropy of cleavage in B.C.C. transition metals, Acta Metall. 21 (1973) 621–627.
[31] L. Giordano, F. Cinquini, G. Pacchioni, Tuning the surface metal work function by deposition of ultrathin oxide films: density functional calculations, Phys. Rev. B 73 (045414) (2005).
[32] N. Hernández, J.A. Sanz, First principles density functional study of Au deposition on TiN (001) surface, Int. J. Mol. Sci. (2001) 263–270.
[33] P. Giannozzi, S. Baroni, N. Bonini, M. Calandra, R. Car, C. Cavazzoni, D. Ceresoli, G.L. Chiarotti, M. Cococcioni, I. Dabo, QUANTUM ESPRESSO: a modular and open-source software project for quantum simulations of materials, J. Phys. Condens. Matter 21 (2009) 395502.
[34] W. Kohn, L.J. Sham, Self-consistent equations including exchange and correlation effects, Phys. Rev. 140 (1965).
[35] J.P. Perdew, K. Burke, M. Ernzerhof, Generalized gradient approximation made simple, Phys. Rev. Lett. 77 (1996) 3865–3868.
[36] A. Kokalj, XCrySDen-a new program for displaying crystalline structures and electron densities, J. Mol. Graph. Model. 17 (1999) 176–179.
[37] G.W. Watson, E.T. Kelsey, N.H. De Leeuw, D.J. Harris, S.C. Parker, Atomistic simulation of dislocations, surfaces and interfaces in MgO, J. Chem. Soc. Faraday Trans. 92 (1996) 433.
[38] J. Greeley, J.K. Nørskov, M. Mavrikakis, Electronic structure and catalysis on metal surfaces, Annu. Rev. Phys. Chem. 53 (2002) 319–348.
[39] J.D. Pack, H.J. Monkhorst, Special points for brillouin-zone integrations-a reply, Phys. Rev. B 16 (1977) 1748–1749.
[41] O. Crisan, A.D. Crisan, Phase transformation and exchange bias effects in mechanically alloyed Fe/magnetite powders, J. Alloys Compd. 509 (2011) 6522–6527.
[42] A. Jain, S.P. Ong, G. Hautier, W. Chen, W.D. Richards, S. Dacek, K.A. Persson, Commentary: the Materials Project: a materials genome approach to accelerating materials innovation, APL Mater. 1 (2013) 1–11 (011002).
[43] P. Błonski,´ A. Kiejna, Structural, electronic, and magnetic properties of bcc iron surfaces, Surf. Sci. 601 (2007) 123–133.
[44] R. Cerf, J. Picard, The Wulff Crystal in Ising and Percolation Models, first ed., Springer-Verlag, Berlin Heidelberg, 2006.
[45] N.H. de Leeuw, C.J. Nelson, A computer modeling study of perfect and defective silver (111) surfaces, J. Phys. Chem. B 107 (2003) 3528–3534.
[47] H. Behner, W. Spiess, G. Wedler, D. Borgmann, Interaction of carbon dioxide with Fe(110), stepped Fe(100) and Fe(111), Surf. Sci. 175 (1986) 276–286.
[48] D.E. Jiang, E.A. Carter, Adsorption and diffusion energetics of hydrogen atoms on Fe(110) from first principles, Surf. Sci. 547 (2003) 85–98.